

Growth of PdCoO₂ films with controlled termination by molecular-beam epitaxy and determination of their electronic structure by angle-resolved photoemission spectroscopy

Cite as: APL Mater. 10, 091113 (2022); <https://doi.org/10.1063/5.0101837>

Submitted: 03 June 2022 • Accepted: 04 August 2022 • Published Online: 22 September 2022

 Qi Song,  Jiaxin Sun,  Christopher T. Parzyck, et al.

COLLECTIONS

Paper published as part of the special topic on [Materials Challenges and Synthesis Science of Emerging Quantum Materials](#)



View Online



Export Citation



CrossMark

ARTICLES YOU MAY BE INTERESTED IN

[Growth of PdCoO₂ by ozone-assisted molecular-beam epitaxy](#)

APL Materials 7, 121112 (2019); <https://doi.org/10.1063/1.5130627>

[In situ x-ray studies of growth of complex oxides on graphene by molecular beam epitaxy](#)

APL Materials 10, 091114 (2022); <https://doi.org/10.1063/5.0101416>

[Large magneto-thermoelectric effect on the verge of metal-insulator and topological transitions in pyrochlore iridates](#)

APL Materials 10, 091111 (2022); <https://doi.org/10.1063/5.0097460>



yttrium iron garnet glassy carbon beamsplitters fused quartz additive manufacturing
zeolites III-IV semiconductors gallium lump copper nanoparticles organometallics
nano ribbons barium fluoride europium phosphors photonics infrared dyes
epitaxial crystal growth ultra high purity materials transparent ceramics CIGS
cerium oxide polishing powder MRE grade materials thin film
surface functionalized nanoparticles sputtering targets fiber optics
OLED lighting solar energy
h-BN deposition slugs CVD precursors photovoltaics
metamaterials borosilicate glass
YBCO superconductors InGaAs
indium tin oxide MgF₂ rutile
diamond micropowder optical glass

The Next Generation of Material Science Catalogs



Growth of PdCoO₂ films with controlled termination by molecular-beam epitaxy and determination of their electronic structure by angle-resolved photoemission spectroscopy

Cite as: APL Mater. 10, 091113 (2022); doi: 10.1063/5.0101837

Submitted: 3 June 2022 • Accepted: 4 August 2022 •

Published Online: 22 September 2022












View Online



Export Citation



CrossMark

Qi Song,¹  Jiaxin Sun,¹  Christopher T. Parzyck,²  Ludi Miao,²  Qing Xu,³ Felix V. E. Hensling,¹  Matthew R. Barone,¹  Cheng Hu,¹ Jinkwon Kim,¹ Brendan D. Faeth,³ Hanjong Paik,³ Phil D. C. King,⁴  Kyle M. Shen,^{2,5}  and Darrell G. Schlom^{1,5,6,a)} 

AFFILIATIONS

¹ Department of Materials Sciences and Engineering, Cornell University, Ithaca, New York 14853, USA

² Department of Physics, Laboratory of Atomic and Solid State Physics, Cornell University, Ithaca, New York 14853, USA

³ Platform for the Accelerated Realization, Analysis, and Discovery of Interface Materials (PARADIM), Cornell University, Ithaca, New York 14853, USA

⁴ SUPA, School of Physics and Astronomy, University of St Andrews, St Andrews KY16 9SS, United Kingdom

⁵ Kavli Institute at Cornell for Nanoscale Science, Ithaca, New York 14853, USA

⁶ Leibniz-Institut für Kristallzüchtung, Max-Born-Straße 2, 12489 Berlin, Germany

Note: This paper is part of the Special Topic on Materials Challenges and Synthesis Science of Emerging Quantum Materials.

^{a)} Author to whom correspondence should be addressed: schlom@cornell.edu

ABSTRACT

Utilizing the powerful combination of molecular-beam epitaxy (MBE) and angle-resolved photoemission spectroscopy (ARPES), we produce and study the effect of different terminating layers on the electronic structure of the metallic delafossite PdCoO₂. Attempts to introduce unpaired electrons and synthesize new antiferromagnetic metals akin to the isostructural compound PdCrO₂ have been made by replacing cobalt with iron in PdCoO₂ films grown by MBE. Using ARPES, we observe similar bulk bands in these PdCoO₂ films with Pd-, CoO₂-, and FeO₂-termination. Nevertheless, Pd- and CoO₂-terminated films show a reduced intensity of surface states. Additionally, we are able to epitaxially stabilize PdFe_xCo_{1-x}O₂ films that show an anomaly in the derivative of the electrical resistance with respect to temperature at 20 K, but do not display pronounced magnetic order.

© 2022 Author(s). All article content, except where otherwise noted, is licensed under a Creative Commons Attribution (CC BY) license (<http://creativecommons.org/licenses/by/4.0/>). <https://doi.org/10.1063/5.0101837>

Metallic oxides with the delafossite structure, shown in Fig. 1(a), have drawn significant attention in recent years due to their unique structural and electronic properties. Examples include PtCoO₂, which has the highest conductivity per carrier of all materials, and PdCoO₂, which has the longest mean free path (exceeding 20 μm at 4 K) among all known metals.¹⁻³ The in-plane electrical conductivity of PdCoO₂ at room temperature, which is about four times higher than that of palladium metal itself, has been argued to arise from electron-phonon scattering mainly occurring

within a single, closed, highly dispersive band of primarily palladium character at the Fermi level (E_F).^{1,4-8} The large spin-splitting of the surface state arising from the CoO₂ termination, in combination with the layered structure of PdCoO₂-based heterostructures makes this system ideal to study itinerant surface electrons driven by inversion-symmetry breaking.⁹ As for the magnetic properties of delafossites, PdCrO₂ is the only highly conducting delafossite material that orders magnetically; it orders antiferromagnetically (AFM) at around 37 K. Focusing on the electronic structure, the single band

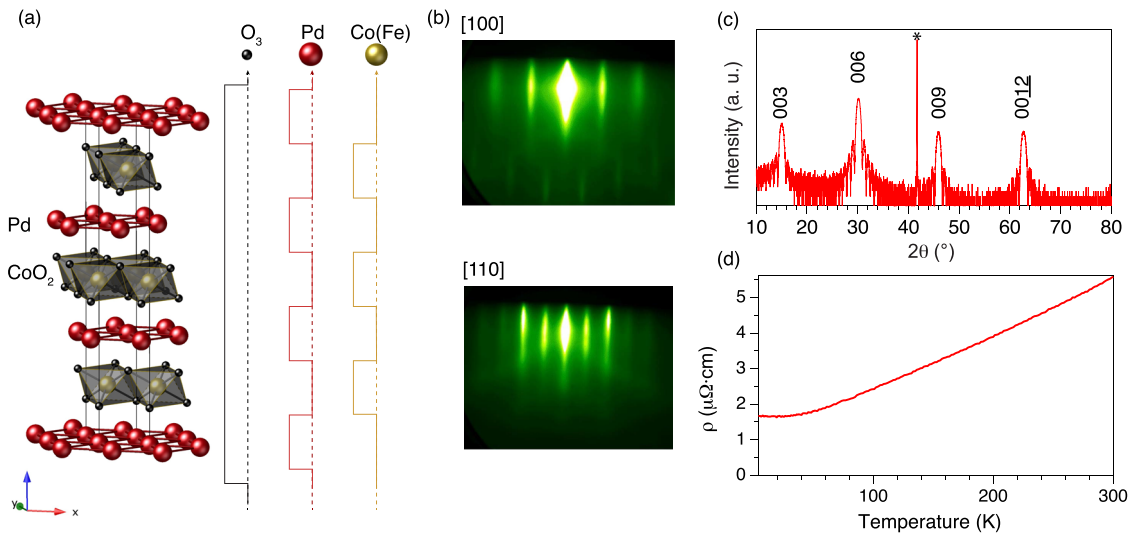


FIG. 1. Structural and electrical characterization of PdCoO₂ thin films grown by MBE on (001) Al₂O₃ substrates. (a) Crystal structure of PdCoO₂ and the shutter timing diagram used for the growth of PdCoO₂. (b) *In-situ* RHEED pattern of PdCoO₂ thin film with a CoO₂ termination viewed along the azimuths indicated. (c) X-ray diffraction of a 12.3 nm thick PdCoO₂ thin film. (d) Resistivity vs temperature of a 52.1 nm thick PdCoO₂ film. * = 006 peak of (001) Al₂O₃ substrate peak.

at the Fermi level with palladium character forms a reconstruction driven by the AFM order from the adjacent CrO₂ layer.^{10–14} Comparing AFM PdCrO₂ with nonmagnetic PdCoO₂, the spins from Cr³⁺ interacting inside the CrO₂ layer with the palladium monolayers on either side of the CrO₂ layer play a critical role in the magnetic state of PdCrO₂.¹³

Angle-resolved photoemission spectroscopy (ARPES) is the premiere experimental tool to directly observe electronic structure in quantum materials. The combination of oxide molecular-beam epitaxy (MBE) with ARPES allows us to customize and study the electronic structure of correlated oxides. This setup has enabled understanding of how strain,^{15,16} thickness,^{17–19} heterostructuring,^{20,21} interfaces,^{22,23} and terminations^{24–29} can influence the electronic structure of thin films.

Due to the limited size of delafossite single crystals, the desire to explore the potential of metallic delafossites in electronic³⁰ and spintronic devices,³¹ together with the exciting opportunities that can be explored in delafossite heterostructures, metallic delafossites are being grown in thin-film form by reactive sputtering,³² pulsed-laser deposition (PLD),^{30,33–36} and MBE.^{37,38} Unfortunately, the transport properties of these films (so far) pale in comparison to the single crystals. Differences between the Fermi surface of the so-called Pd-terminated PdCoO₂ with CoO₂-terminated PdCoO₂ have recently been reported for epitaxial films of PdCoO₂ grown by PLD.³⁹ The claims of this prior study would be strengthened by improved evidence of surface termination control.

In this work, we describe an improved synthetic strategy for the growth of PdCoO₂ films with control of surface termination by MBE. Harnessing the ultra-high vacuum connection between our MBE and ARPES, we then study the electronic structure of Pd-terminated and CoO₂-terminated PdCoO₂. We find that our PdCoO₂ films exhibit similar bulk bands derived from palladium states but weak surface states compared to those in PdCoO₂ single

crystals. Having succeeded in engineering the surface termination in PdCoO₂ over large areas, we then progress to investigate terminations of PdCoO₂ where we deliberately add unpaired electrons and study the resulting electronic structure by ARPES. Although we are able to epitaxially stabilize a variety of surface terminations involving iron substituting for cobalt in PdCoO₂, we do not see evidence of magnetic order.

Building upon our previous work,³⁸ thin films of PdCoO₂ were synthesized by MBE in a Veeco GEN10 MBE system on (001) sapphire substrates. Details of the film growth are provided in the [supplementary material](#). Figure 1(a) shows the shutter timing diagram used to supply fluxes of the individual molecular beams to the substrate to form PdCoO₂. After growth, films were cooled down to 300 °C in the same ozone background pressure (around 5×10^{-6} Torr) in which they were grown and transferred under ultra-high vacuum conditions into an adjacent ARPES chamber. The reflection high-energy electron diffraction (RHEED) patterns acquired after deposition and the x-ray diffraction θ - 2θ scans indicate the growth of single-phase PdCoO₂ films as shown in Figs. 1(b) and 1(c). The structure was characterized by a Panalytical Empyrean x-ray diffractometer utilizing Cu K α_1 radiation. Electrical transport measured by a Quantum Design Physical Property Measurement System (PPMS) using a four-point van der Pauw geometry is shown in Fig. 1(d). The residual resistivity ratio (RRR = ρ_{300K}/ρ_{4K}) of this PdCoO₂ sample with a thickness of 52.1 nm is 3.3 in its as-grown state (i.e., no *ex-situ* postanneal). For comparison, the highest RRR previously achieved by MBE for a film in its as-grown state was 2.2 for a 10 nm thick PdCoO₂ film.³⁸ After an *ex-situ* anneal, films grown by MBE can reach a RRR of around 8 for a 50 nm thick PdCoO₂ film.³⁷ While these are the highest reported RRR values for films, PdCoO₂ single crystals can exhibit RRR as high as 400.¹ The resistivity of epitaxial PdCoO₂ films and single crystals are comparable at room temperature;

the huge difference in resistivity emerges upon cooling. One likely defect responsible for this difference is the in-plane rotation twins present in all epitaxial delafossite films to date. The presence of 180° in-plane rotation twins in PdCoO₂ film grown on (001) Al₂O₃ substrates manifest in the x-ray ϕ scan and scanning transmission electron microscopy images shown in Ref. 38, as well as the atomic force microscopy images shown in the [supplementary material](#) (Fig. S3).

In situ ARPES measurements are performed to study the effects of termination on the electronic structure of the PdCoO₂ films. Our lab-based ARPES system photoexcites electrons with a Scienta omicron VUV 5000 helium discharge lamp using He-I photons at 21.2 eV and He-II photons at 40.4 eV. The emitted electrons are detected with a VG Scienta R4000 electron analyzer. The ARPES is vacuum-connected to the MBE growth chamber via an ultra-high vacuum transfer chamber.

We first compare the Fermi surface of Pd-terminated and CoO₂-terminated PdCoO₂ films in Figs. 2(a) and 2(b), respectively. The sharp hexagonal pocket centered at Γ [illustrated in red in Figs. 2(a) and 2(b)] is observed in both Pd- and CoO₂-terminated PdCoO₂ films. Two smaller hexagonal pockets inside the bulk state pocket illustrated in green and blue are observed in the CoO₂-terminated PdCoO₂ film, in agreement with previous reports of splitting of the CoO₂ surface state driven by spin-orbit coupling.^{40,41} For Pd-terminated PdCoO₂, we do not observe pronounced palladium surface states at E_F . Below E_F , however, there is some spectral weight possibly from the palladium surface state as described in Ref. 41. At He-II photon energy (40.4 eV), we observe stronger spectral weight below E_F , as illustrated in Fig. S5 of the [supplementary material](#). This intensity below E_F might be related to the palladium surface state, but at this higher energy, still no palladium surface state appears at E_F .

In Figs. 3(a) and 3(c), we further compare the dispersion cut along the Γ -K direction of Pd- and CoO₂-terminated PdCoO₂, respectively. The fitted Fermi velocities (v_F s) of the PdCoO₂ bulk state of Pd- and CoO₂-terminated films are all around 4.5 eV \AA , as shown in Table I, in agreement with previous results measured on PdCoO₂ single crystals by ARPES.^{9,13} Despite the invisible palladium surface state at E_F , two spin-split surface states from the CoO₂ termination show up at E_F . These are indicated by blue and green circles in Fig. 3(c). From the momentum dispersion curves (MDCs) comparison of Pd- and CoO₂-terminated samples in Fig. 3(e), it is easier to observe the CoO₂ surface states at E_F (indicated by the blue arrows) and very little of the palladium surface state is observed below E_F (indicated by the red arrow). The Fermi velocities of the CoO₂ surface states are 0.75 eV \AA (blue) and 0.5 eV \AA (green), respectively. This is roughly 10% of that of the bulk state, in agreement with the previous study of PdCoO₂ single crystals.^{9,42} Dispersion along the K-M-K direction of Pd- and CoO₂-terminated PdCoO₂ films are shown in Figs. 3(f) and 3(h). Both terminations of the PdCoO₂ films show a split band at the M point 0.75 eV below E_F and 1.75 eV below E_F , as observed in PdCoO₂ single crystals.⁴¹ Interestingly, a hole band below E_F at the M point driven by the palladium surface state (as shown in Ref. 41) is not seen in our Pd-terminated films.

Comparing the electronic structure observed for our epitaxial PdCoO₂ thin films to that reported for PdCoO₂ single crystals with different terminations, our PdCoO₂ films have similar bulk state features to those of PdCoO₂ single crystals, but the surface states of our PdCoO₂ films are weaker or even disappear at E_F . Note that the alternating layers of Pd⁺ and CoO₂⁻ along the *c*-axis of PdCoO₂ are not charge neutral. Doping of the surface by electrons arising from electronic reconstruction (i.e., no structural surface reconstruction) would generate the surface states observed on bulk single crystals.

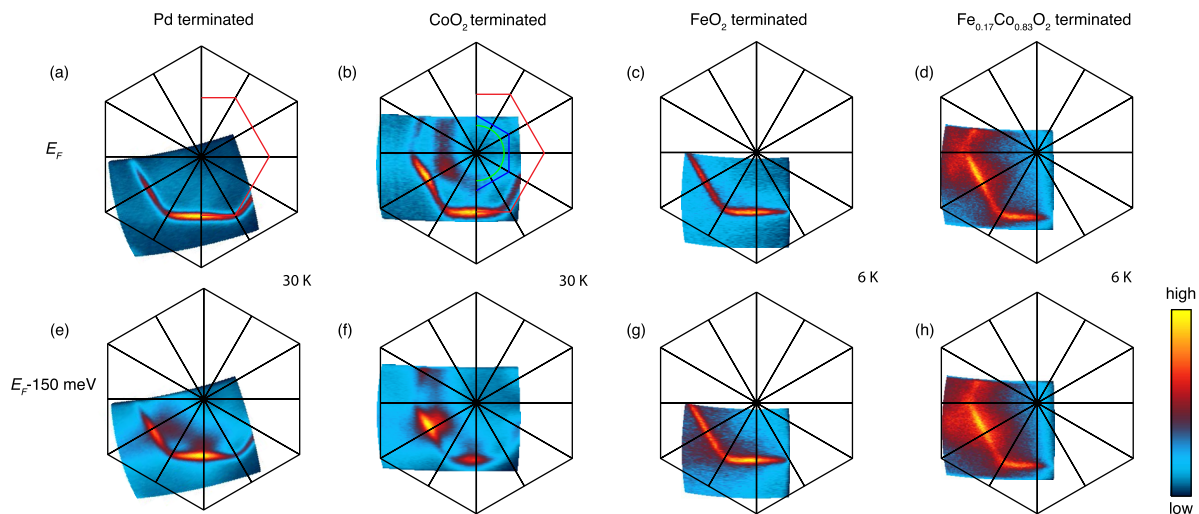


FIG. 2. Photoemission intensity maps at the Fermi energy ± 5 meV of (a) a Pd-terminated 18 nm thick PdCoO₂ film, (b) CoO₂-terminated 12 nm thick PdCoO₂ film, (c) a FeO₂-terminated 13 nm thick PdCoO₂ film, and (d) a Fe_{0.17}Co_{0.83}O₂-terminated 13 nm thick PdCoO₂ thin film. The PdCoO₂ bulk state is illustrated by the incomplete red hexagon in (a) and (b). The surface states of CoO₂ are exhibited in the incomplete blue hexagon and green circle in (b). (e)–(h) The same as (a)–(d) but taken at 150 meV below the Fermi energy. (a), (b), (e), (f) were taken at 30 K; (c), (d), (g), (h) were taken at 6 K. All data were measured using a photon energy of 21.2 eV.

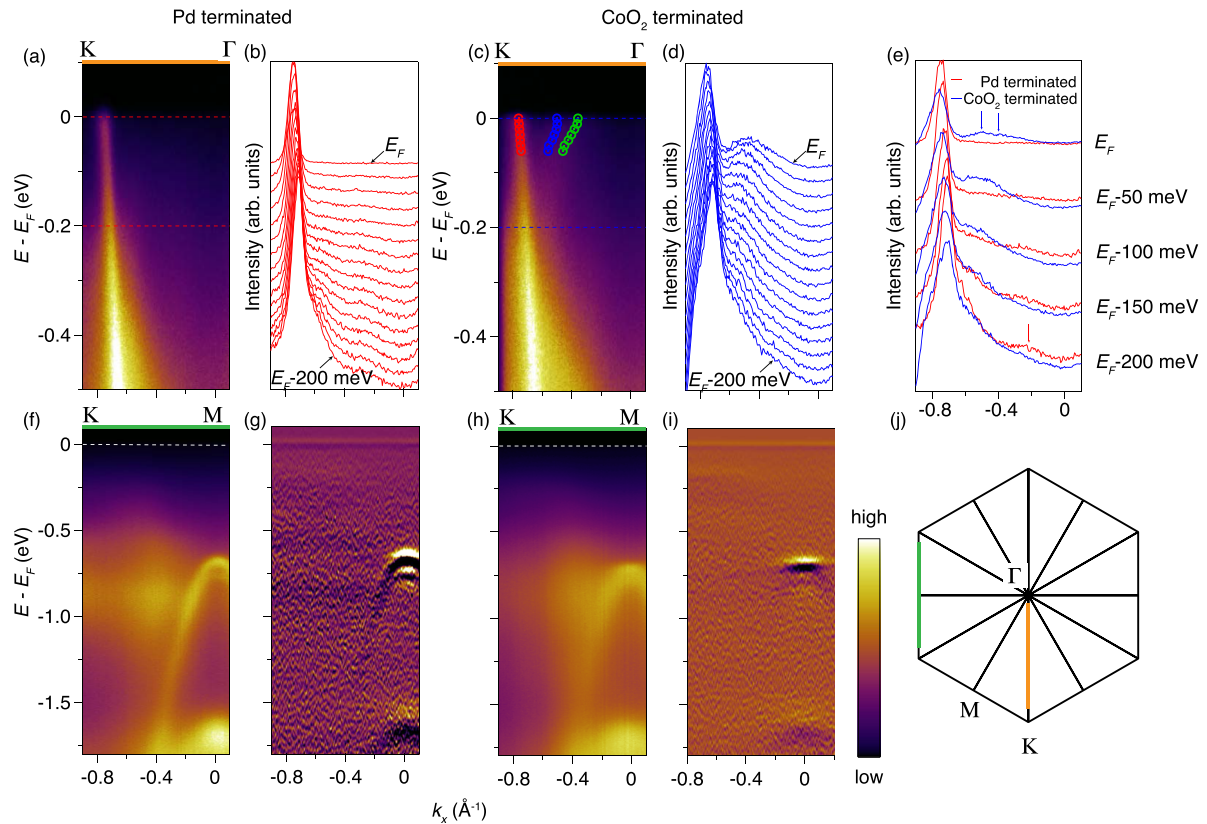


FIG. 3. Photoemission intensity distribution of Pd- and CoO_2 -terminated PdCoO_2 films measured at a photon energy of 21.2 eV at 30 K. (a) Photoemission intensity distributions across Γ -K along the orange cut illustrated in (j) of the Pd-terminated PdCoO_2 film in Fig. 2(a). (b) Momentum dispersion curves (MDCs) at E_F to $E_F - 0.2$ eV illustrated by the red dash lines in (a). (c) and (d) The same as (a) and (b), but taken from the CoO_2 -terminated PdCoO_2 film in Fig. 2(b). The red, blue, and green circles in (c) indicate fitted peak positions of the PdCoO_2 bulk state and surface states from the MDC near E_F . Fitting details are shown in Fig. S6 of the supplementary material. (e) MDC comparison of the cut along the Γ -K direction at various energies. The blue arrows on the top indicate the extra peaks in the CoO_2 -terminated PdCoO_2 film. The red arrow below E_F indicates the weak palladium surface state peak in the Pd-terminated PdCoO_2 film. (f) Photoemission spectra along K-M-K of the Pd-terminated PdCoO_2 film and its second derivative with respect to energy (g). (h) and (i) The same as (f) and (g), but taken from the same CoO_2 -terminated PdCoO_2 film.

Ways in which the surfaces of our films differ from the single crystals provide routes to different or no surface states. For ARPES measurements of cleaved (001)-oriented PdCoO_2 single crystals, the polar surface exposed after cleaving may drive an electronic reconstruction of the surface or alternatively a mixture of termination regions, some of which are terminated by palladium and some of which are terminated by CoO_2 , to alleviate the polar surface charge. To synthesize PdCoO_2 films, we use shuttered MBE growth to provide a full layer of palladium or CoO_2 as the terminating surface. This difference in the surface reconstruction structure of epitaxial PdCoO_2 films might result in a different electronic reconstruction from that

of cleaved PdCoO_2 single crystals. We show the reconstruction of our films in low-energy electron diffraction (LEED) with different terminations in Fig. S4 of the supplementary material. Additional differences exist between our PdCoO_2 films and PdCoO_2 single crystals. For example, PdCoO_2 films grown on (001) Al_2O_3 substrates are known to have a high density of 180° in-plane rotation twins.³⁸ Furthermore, our films might contain oxygen vacancies to neutralize the surface polar effect. These may also play a role in the differences observed in the surface states between PdCoO_2 single crystals and our epitaxial films. In particular, the palladium surface state is very reactive; it can be essentially destroyed by temperature cycling of ARPES measurements.⁴² Prior ARPES results of a PdCoO_2 film grown by PLD,³⁹ where the palladium termination is confirmed by the absence of a CoO_2 surface state in the electronic structure, does not show the PdCoO_2 bulk state. In contrast, our Pd-terminated films show a strong PdCoO_2 bulk state without a CoO_2 surface state, but are missing the palladium surface state. One possible reason for this is the difference in sample quality, particularly of the sample surface and the ability of MBE to control the termination

TABLE I. Fermi velocities of the bulk states of PdCoO_2 from fitting the ARPES spectra of PdCoO_2 films.

Fermi Velocity	Pd	CoO_2	FeO_2	$\text{Fe}_{0.17}\text{Co}_{0.83}\text{O}_2$
v_F (eV \AA)	4.72 ± 0.15	4.32 ± 0.25	4.69 ± 0.07	4.43 ± 0.09

of the PdCoO₂ film. We note that our MBE and ARPES measurements are made immediately following film growth and that the ultra-high vacuum connection between our MBE and ARPES systems enables us to investigate the electronic structure of the pristine growth surface.

With the goal of introducing magnetic order into the surface of PdCoO₂, we attempt to replace the cobalt in the CoO₂ surface termination with a different transition metal. The low spin state ($S = 0$) of the d^6 electron configuration of Co³⁺ in octahedral coordination underlies the lack of magnetic order in PdCoO₂. In contrast, PdCrO₂ is known to order antiferromagnetically at 37 K due to the unpaired spins ($S = 3/2$) arising from Cr³⁺ with its d^3 electron configuration.^{10,11} Considering what other transition metals are stable in the 3+ oxidation state under the highly oxidizing conditions needed to stabilize PdCoO₂ led us to attempt to substitute Fe³⁺ for Co³⁺. Other known iron-containing delafossites, such as the semiconductors AgFeO₂ and CuFeO₂ with bandgap larger than 1 eV, are known to exhibit magnetic phase transitions.^{43–46} Combining magnetic FeO₂ with conducting palladium might create a new metallic delafossite with interesting magnetic properties. Note that PdFeO₂ is neither a known compound nor has it been suggested to form in the delafossite structure by prior crystal chemistry based suggestions of delafossites^{47,48} nor first-principles suggestions for new delafossites.^{49,50}

Our attempts to terminate PdCoO₂ with a monolayer of FeO₂ were successful. To do so, we used epitaxial stabilization, a process in which lattice misfit strain energies and interfacial energies are exploited to favor a desired metastable phase over the equilibrium phase.^{51–56} ARPES measurements reveal the FeO₂-terminated PdCoO₂ film to have a similar bulk band to PdCoO₂, but there is no

extra surface state at the Fermi surface nor a reconstruction driven by AFM order like in PdCrO₂. In addition, we synthesized Pd(Co, Fe)O₂ films containing a solid solution of iron and cobalt in each CoO₂ layer of the Pd(Co,Fe)O₂ film. Electrical transport measurements on a series of 13 nm thick PdFe_xCo_{1-x}O₂ films with varying x ($0 < x \leq 0.2$) all show a drop in resistance at low temperature. Other than the dip shown in $d\rho/dT$ at low temperature, which is different from other known delafossites, no pronounced magnetic order is observed by magnetic susceptibility measurement down to 3 K. This behavior is in contrast to what is seen for PdCrO₂. Turning to the electronic structure of the PdFe_xCo_{1-x}O₂ films revealed by ARPES, a similar bulk band to PdCoO₂ is observed. No reconstruction appears at the Fermi surface nor is any temperature dependence of the electronic structure of PdFe_xCo_{1-x}O₂ seen.

We added a full monolayer of FeO₂ to a Pd-terminated PdCoO₂ film in an attempt to vary the termination of PdCoO₂ by introducing unpaired electrons (spin) from Fe³⁺. As ARPES is a surface sensitive measurement, if the unpaired electrons from Fe³⁺ with its d^5 configuration in the surface FeO₂ layer interact within the FeO₂ layer and with the adjacent palladium layer like the CrO₂ layer does in the AFM metal PdCrO₂,¹³ we expect to see distinct features arise in the Fermi surface of the FeO₂-terminated PdCoO₂ film. The well crystallized FeO₂ termination determined by RHEED is shown in Fig. 5(a). Unfortunately, no difference is observed in the ARPES other than the similar PdCoO₂ bulk state appearing at the Fermi surface in the FeO₂-terminated PdCoO₂ film, as shown in Figs. 2(c) and 2(g). No reconstruction of the Fermi surface was seen at low temperature. The bulk band was also free of any temperature-dependent features when we analyzed the MDCs in the Γ -K direction shown in Fig. 4(e). Thus, our epitaxial FeO₂ layer on the surface of PdCoO₂

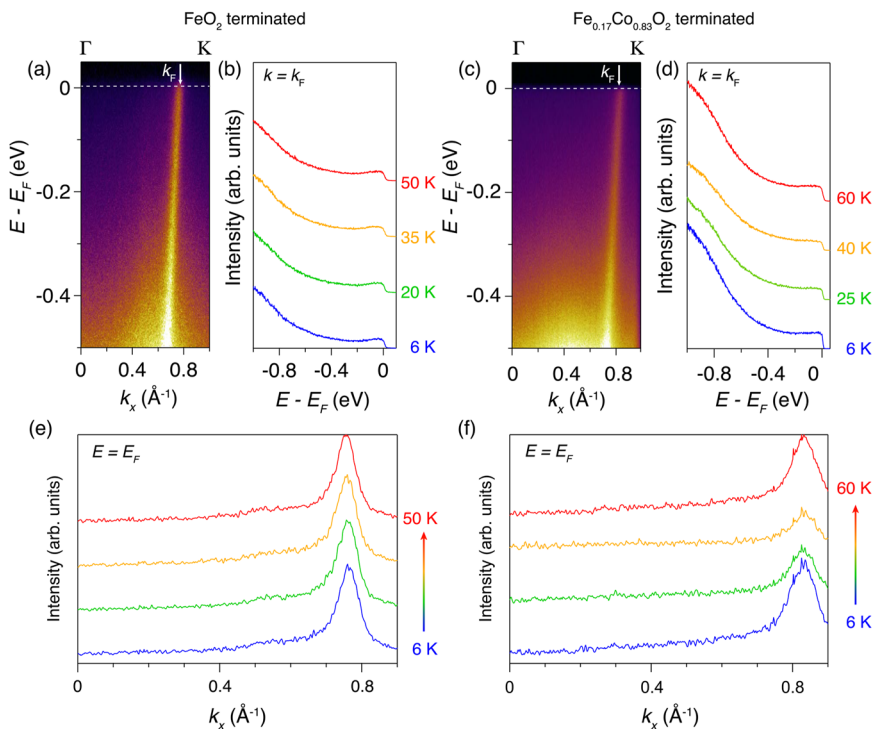


FIG. 4. Photoemission intensity distribution of FeO₂- and Fe_{0.17}Co_{0.83}O₂-terminated PdCoO₂ films and their temperature dependence. (a) Photoemission intensity distributions across Γ -K along the orange cut illustrated in Fig. 3(j) of the FeO₂-terminated PdCoO₂ film in Fig. 2(c). (b) Temperature dependence of the energy dispersion curves (EDCs) of k_F illustrated in (a). (c) and (d) The same as (a) and (b), but are taken from the Fe_{0.17}Co_{0.83}O₂-terminated PdCoO₂ film in Fig. 2(d). (e) Temperature dependence of the momentum dispersion curves (MDCs) at E_F for the FeO₂-terminated film. (f) The same as (e), but for the Fe_{0.17}Co_{0.83}O₂-terminated PdCoO₂ film.

film does not appear to create a spin interaction with the underlying palladium layer. On the other hand, PdFeO₂ is a metastable phase and we can only stabilize one formula unit of PdFeO₂. It is possible that the FeO₂ termination is insulating due to oxygen vacancies to neutralize its otherwise polar surface and preventing it from contributing to the electronic structure. The photoemission intensity data we collect include the film beneath the FeO₂ layer, which is PdCoO₂ itself.

In addition to replacing the entire CoO₂ monolayer with an FeO₂ monolayer, we also investigated the partial replacement of cobalt with iron hoping that the presence of iron in multiple layers of the Pd(Co,Fe)O₂ structure would enhance the chance of spin interaction between the Fe³⁺ and the adjacent palladium layer. In Figs. 2(d) and 2(h), one can observe that the band of the PdFe_{0.17}Co_{0.83}O₂ film still has similar features to the bulk state of PdCoO₂, but with significant noise. Meanwhile, similar to the FeO₂-terminated PdCoO₂ film, no temperature dependence of the bulk band of Pd(Co,Fe)O₂ is seen at E_F [see Figs. 4(c)–4(f)]. We compared the Fermi velocity (v_F) of the PdFe_{0.17}Co_{0.83}O₂ film with the other three different terminations of PdCoO₂ films in Table I, and within experimental error, they all have the same v_F value as that of PdCoO₂ single crystals.⁴¹ Thus, the partial replacement of cobalt by iron in each CoO₂ layer does not bring any ordered spin interaction between the (Co,Fe)O₂ layers nor do we observe any evidence of interaction with the electrons of Pd(Co,Fe)O₂, which contribute to the bulk band of PdCoO₂. The noise observed in the Fermi surface of the PdFe_{0.17}Co_{0.83}O₂ film might come from the increased disorder accompanying the replacement of cobalt by iron. With the d^5 configuration of Fe³⁺ and the d^6 configuration of Co³⁺, the Fe_{0.17}Co_{0.83}O₂ layer should, in principle, have a $d^{5.83}$ configuration

resulting in unfilled d electron bands. Nonetheless, no new conducting band is seen at E_F as shown in Fig. 4. On the other hand, a hole doping scenario in which 0.17 electrons move from the palladium layer to the Fe_{0.17}Co_{0.83}O₂ layer would leave the Fe_{0.17}Co_{0.83}O₂ layer in an insulating state. Such a scenario would require hole doping of 0.17 holes on the palladium layer. A comparison of the momentum at E_F (k_F) shown in Fig. S7 of the supplementary material, reveals no pronounced difference between the k_F s of a PdCoO₂ film and a Fe_{0.17}Co_{0.83}O₂ film.

Further characterization of the PdFe_xCo_{1-x}O₂ films is shown in Fig. 5. The maximum percentage of iron that we are able to incorporate into epitaxial PdFe_xCo_{1-x}O₂ films while retaining a single phase is $x = 20\%$. RHEED of a single-phase, 13 nm thick PdFe_{0.2}Co_{0.8}O₂ film is shown in Fig. 5(a). The fringes in the x-ray diffraction θ - 2θ scans of the PdFe_xCo_{1-x}O₂ films indicate the high structural quality of these films. Electrical transport measurement on the PdFe_xCo_{1-x}O₂ films is shown in Fig. 5(d). Note that the PdCoO₂ film shown in this comparison has a thickness of 13 nm, a quarter of the thickness of the PdCoO₂ film in Fig. 1(d). The upturn in resistivity of the pure PdCoO₂ film (0% Fe) seen in Fig. 5(d) below 20 K likely originates from localization in the ultrathin film. As more cobalt is replaced by iron, the absolute resistivity of the iron-doped PdCoO₂ film keeps increasing. Interestingly, instead of showing an upturn at low temperature like is seen in the pure PdCoO₂ film, the Fe-doped PdCoO₂ films show a drop at low temperature in electrical resistivity. Moreover, as the iron content (x) of the PdFe_xCo_{1-x}O₂ film is increased, a more pronounced drop in resistivity is seen. Derivatives of the resistivity as a function of temperature of these PdFe_xCo_{1-x}O₂ films are shown in Fig. 5(e). Strikingly, a dip at about 20 K is observed in the temperature derivatives of all iron-doped

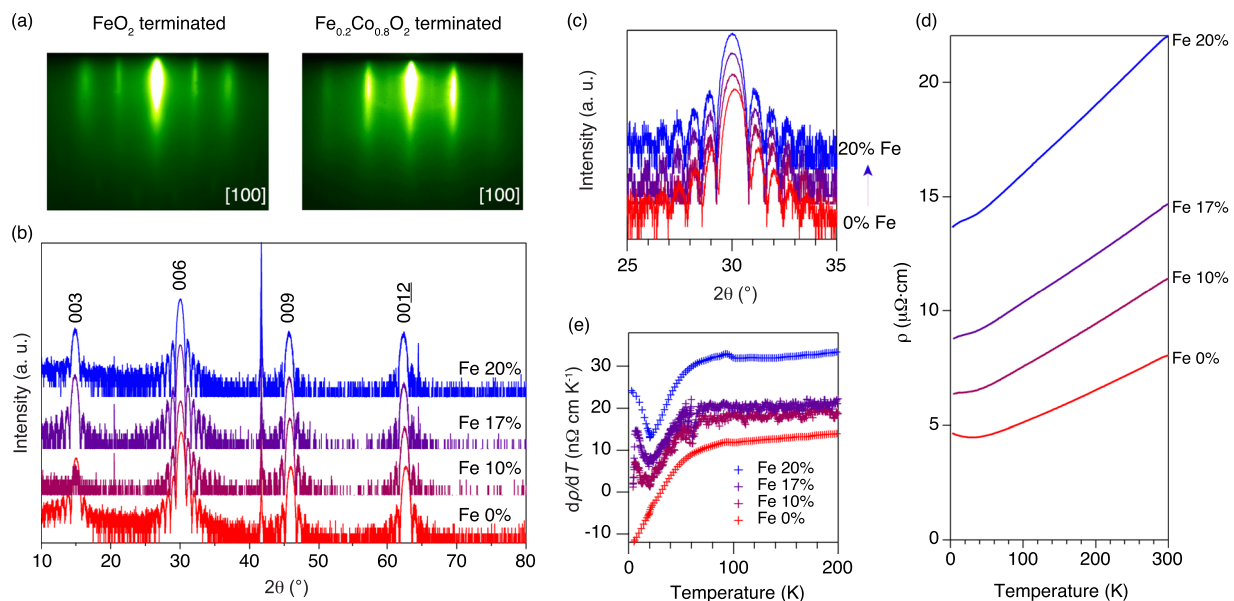


FIG. 5. Structural and electrical characterization of 13 nm thick PdFe_xCo_{1-x}O₂ thin films grown on (001) Al₂O₃ substrates. (a) *In-situ* RHEED pattern of a FeO₂-terminated PdCoO₂ thin film and a PdFe_{0.2}Co_{0.8}O₂ thin film terminated with the Fe_{0.2}Co_{0.8}O₂ layer. (b) X-ray diffraction of a series of PdFe_xCo_{1-x}O₂ thin films with x ranging from 0 to 0.2. (c) Close-up of the 006 reflection in (b). (d) Resistivity vs temperature of the PdFe_xCo_{1-x}O₂ thin films shown in (b). (e) Derivative of the film resistivity with respect to temperature as a function of temperature of these same PdFe_xCo_{1-x}O₂ thin films. * = 006 peak of the (001) Al₂O₃ substrate.

PdCoO₂ films, which is opposite to the dp/dT in PdCrO₂ where a peak shows up at T_N driven by AFM order.¹⁰ The amplitude of the dip observed for PdFe_xCo_{1-x}O₂ increases with larger iron concentration.

A comparison of the temperature dependence of the Hall coefficient (R_H) between a PdCoO₂ film and a PdFe_{0.17}Co_{0.83}O₂ film is shown in Fig. 6(a). The R_H measurements are consistent with electrons acting as the carriers in both PdCoO₂ and PdFe_{0.17}Co_{0.83}O₂ films. The magnitude of R_H in the PdCoO₂ film is in agreement with prior reports from PdCoO₂ single crystals.⁵⁷ In contrast to Ref. 39, we do not observe an anomalous Hall effect in our PdCoO₂ films at low temperature. Hall resistivities of the PdCoO₂ film and the PdFe_{0.17}Co_{0.83}O₂ film are shown in Fig. S9 of the [supplementary material](#). The PdFe_{0.17}Co_{0.83}O₂ film exhibits a larger R_H than does the pure PdCoO₂ film, which could be a result of carriers being trapped by iron-induced structural defects. For the PdCoO₂ film, the temperature dependence of R_H at low temperature becomes flat while for the iron-doped PdCoO₂ film the R_H starts increasing below 20 K, which is the same temperature at which the change in dp/dT is observed in Fig. 5. One possibility for the observed resistivity anomaly at low temperature is that it is driven by iron disorder, since it is independent of the iron concentration. One scenario explaining why the R_H difference between of PdCoO₂ film and the PdFe_{0.17}Co_{0.83}O₂ film does not reflect on the band structure is that the electrons from iron do not interact with the electrons from palladium. Instead, iron clusters just trap the electrons from the PdCoO₂. Within this scenario, it is possible that iron disorder clusters in PdFe_{0.17}Co_{0.83}O₂ films are revealed by AFM in the [supplementary material](#) (Fig. S3). In Figs. 6(c) and 6(d), the magnetoresistance of the same PdCoO₂ film and PdFe_{0.17}Co_{0.83}O₂ film shows distinct

magnetic dependences. The overall scale of magnetoresistance in the PdCoO₂ film is much smaller than that observed in PdCoO₂ single crystals.⁵⁸ The temperature dependence of the magnetoresistance of the PdFe_{0.17}Co_{0.83}O₂ film shows weak-localization-like behavior, which may arise from the magnetic disorder resulting from the addition of iron. The temperature dependence of the magnetic susceptibility of the PdFe_{0.17}Co_{0.83}O₂ thin film shows no transition or difference between the zero-field-cooled (ZFC) and field-cooled (FC) curves as shown in the [supplementary material](#) (Fig. S10). The observed behavior is in contrast to the splitting that is expected when AFM order is observed, such as in PdCrO₂.¹¹ Thus, the replacement of cobalt by iron does not appear to result in any spin order. Instead, only signs of magnetic disorder are seen.

In summary, we have synthesized high-quality PdCoO₂ films by MBE and harnessed the atomic layer control afforded by MBE to tune the termination of these films to study the resulting electronic structure by ARPES. On comparing the Pd-terminated and CoO₂-terminated PdCoO₂ films with those of PdCoO₂ single crystals, though the resistivity of our PdCoO₂ films are far higher than that of single crystals at low temperature, we find the PdCoO₂ bulk states in our films show features similar to those of PdCoO₂ single crystals, while the palladium surface state and CoO₂ surface state are not as strong as those of the PdCoO₂ single crystals. This difference might arise due to different electronic reconstructions. We also studied FeO₂-terminated PdCoO₂ films and find that the only remaining PdCoO₂ bulk state in the electronic structure is similar to that of PdCoO₂. In addition, we have successfully synthesized PdFe_xCo_{1-x}O₂ films. From the electric transport measurements, the addition of iron further increases the resistivity of PdCoO₂ films at room temperature. Meanwhile, we see different behavior at low

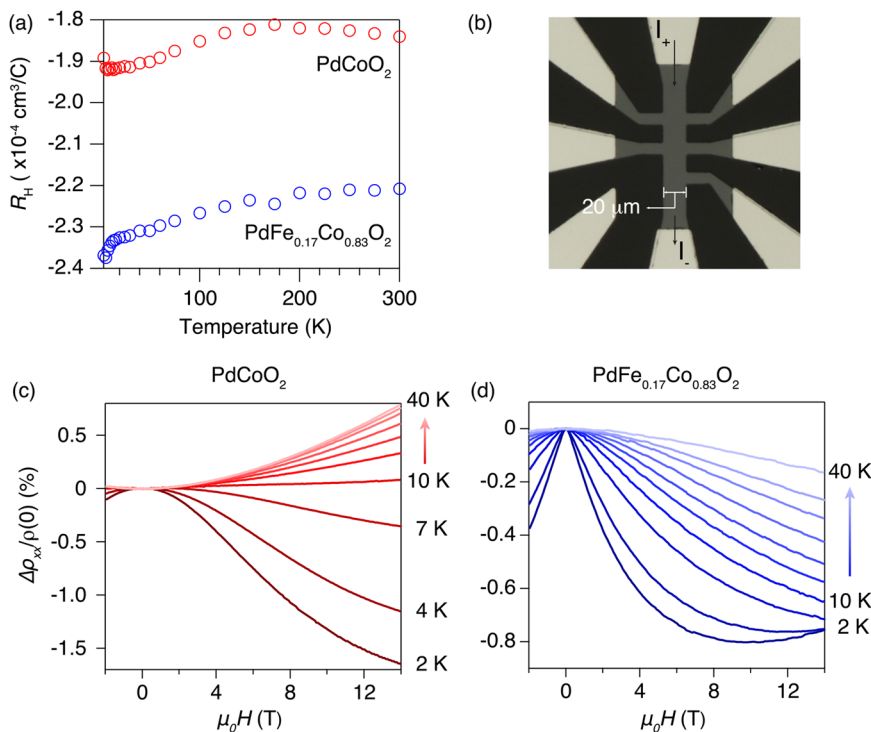


FIG. 6. (a) Hall coefficient of a 13.5 nm thick PdCoO₂ film and a 13.1 nm thick PdFe_{0.17}Co_{0.83}O₂ film. (b) Geometry of the Hall bar. The dimension of the channel is 20 μm . (c) and (d) $\Delta\rho/\rho(0)$ vs magnetic field of the same PdCoO₂ and the PdFe_{0.17}Co_{0.83}O₂ films, respectively.

temperature compared to pure PdCoO₂ films, but no magnetic ordering akin to what happens in PdCrO₂ is seen in our PdFe_xCo_{1-x}O₂ films. The electronic structure of a PdFe_{0.17}Co_{0.83}O₂ film shows a bulk state similar to that seen in pure PdCoO₂ films. Although we do not induce new spin order in delafossite films by replacing cobalt by iron in PdFe_xCo_{1-x}O₂ with x up to 0.2 or a pure FeO₂ terminating monolayer, our work invites further exploration of ways in which the electronic structure of delafossites can be perturbed by exploiting the ability of MBE to control atomic layering in combination with ARPES to measure its impact.

See the [supplementary material](#) for the growth methods of the PdFe_xCo_{1-x}O₂ ($0 \leq x \leq 0.2$) films and additional characterization by AFM, LEED, ARPES, and XPS, as well as the results of Hall effect and magnetization measurements.

The authors thank Alfred Zong, Juan Jiang, Yu He, and Ligu Ma for their insightful discussions. This paper was primarily supported by the U.S. Department of Energy, office of Basic Sciences, Division of Materials Science and Engineering under Award No. DE-SC0002334. This paper made use of the Cornell Center for Materials Research shared facilities, which are supported through the NSF Materials Research Science and Engineering Centers Program (Grant No. DMR-1719875). This paper also made use of the Cornell Energy Systems Institute Shared Facilities partly sponsored by the NSF (Grant No. MRI DMR-1338010) and the Kavli Institute at Cornell. Substrate preparation was performed, in part, at the Cornell NanoScale Facility, a member of the National Nanotechnology Coordinated Infrastructure, which is supported by the NSF (Grant No. NNCI-2025233). C.T.P. acknowledges support from Air Force Office of Scientific Research Grant No. FA9550-21-1-0168 and National Science Foundation Grant No. DMR-2104427. P.D.C.K. gratefully acknowledges support from the European Research Council (through the QUESTDO project, Grant No. 714193). Q.X. acknowledges support from the REU Site: Summer Research Program at PARADIM (Grant No. DMR-2150446). The authors thank Sean C. Palmer for his assistance with substrate preparation.

AUTHOR DECLARATIONS

Conflict of Interest

The authors have no conflicts to disclose.

Author Contributions

Qi Song: Conceptualization (equal); Data curation (equal); Formal analysis (equal); Writing – original draft (equal). **Brendan D. Faeth:** Data curation (supporting). **Hanjong Paik:** Data curation (supporting). **Phil D. C. King:** Writing – review & editing (supporting). **Kyle M. Shen:** Resources (equal). **Darrell G. Schlom:** Conceptualization (equal); Data curation (supporting); Funding acquisition (lead); Project administration (equal); Resources (equal); Writing – review & editing (equal). **Jiaxin Sun:** Data curation (equal); Writing – review & editing (supporting). **Christopher T. Parzyck:** Formal analysis (supporting); Writing – review & editing (equal). **Ludi Miao:** Data curation (equal); Writing – review & editing (supporting). **Qing Xu:** Data curation (supporting). **Felix V.E. Hensling:**

Data curation (supporting). **Matthew R. Barone:** Data curation (supporting); Formal analysis (supporting); Writing – review & editing (supporting). **Cheng Hu:** Data curation (supporting). **Jinkwon Kim:** Data curation (supporting).

DATA AVAILABILITY

The data that support the findings of this study are available from the corresponding author upon reasonable request.

REFERENCES

- C. W. Hicks, A. S. Gibbs, A. P. Mackenzie, H. Takatsu, Y. Maeno, and E. A. Yel'land, "Quantum oscillations and high carrier mobility in the delafossite PdCoO₂," *Phys. Rev. Lett.* **109**, 116401 (2012).
- P. Kushwaha, V. Sunko, P. J. Moll, L. Bawden, J. M. Riley, N. Nandi, H. Rosner, M. P. Schmidt, F. Arnold, E. Hassinger, T. K. Kim, M. Hoesch, A. P. MacKenzie, and P. D. King, "Nearly free electrons in a 5d delafossite oxide metal," *Sci. Adv.* **1**, e1500692 (2015).
- A. P. Mackenzie, "The properties of ultrapure delafossite metals," *Rep. Prog. Phys.* **80**, 032501 (2017).
- V. Eyert, R. Frésard, and A. Maignan, "On the metallic conductivity of the delafossites PdCoO₂ and PtCoO₂," *Chem. Mater.* **20**, 2370–2373 (2008).
- K. Kim, H. C. Choi, and B. I. Min, "Fermi surface and surface electronic structure of delafossite PdCoO₂," *Phys. Rev. B* **80**, 035116 (2009).
- K. P. Ong, D. J. Singh, and P. Wu, "Unusual transport and strongly anisotropic thermopower in PtCoO₂ and PdCoO₂," *Phys. Rev. Lett.* **104**, 176601 (2010).
- K. P. Ong, J. Zhang, J. S. Tse, and P. Wu, "Origin of anisotropy and metallic behavior in delafossite PdCoO₂," *Phys. Rev. B* **81**, 115120 (2010).
- R. Daou, R. Frésard, S. Hébert, and A. Maignan, "Large anisotropic thermal conductivity of the intrinsically two-dimensional metallic oxide PdCoO₂," *Phys. Rev. B* **91**, 041113 (2015).
- V. Sunko, H. Rosner, P. Kushwaha, S. Khim, F. Mazzola, L. Bawden, O. J. Clark, J. M. Riley, D. Kasinathan, M. W. Haverkort, T. K. Kim, M. Hoesch, J. Fujii, I. Vobornik, A. P. Mackenzie, and P. D. C. King, "Maximal Rashba-like spin splitting via kinetic-energy-coupled inversion-symmetry breaking," *Nature* **549**, 492–496 (2017).
- H. Takatsu, H. Yoshizawa, and Y. Maeno, "Comparative study of conductive delafossites with and without frustrated spins on a triangular lattice, PdMO₂ (M = Cr; Co)," *J. Phys.: Conf. Ser.* **145**, 012046 (2009).
- H. Takatsu and Y. Maeno, "Single crystal growth of the metallic triangular-lattice antiferromagnet PdCrO₂," *J. Cryst. Growth* **312**, 3461–3465 (2010).
- H.-J. Noh, J. Jeong, B. Chang, D. Jeong, H. S. Moon, E.-J. Cho, J. M. Ok, J. S. Kim, K. Kim, B. I. Min, H.-K. Lee, J.-Y. Kim, B.-G. Park, H.-D. Kim, and S. Lee, "Direct observation of localized spin antiferromagnetic transition in PdCrO₂ by angle-resolved photoemission spectroscopy," *Sci. Rep.* **4**, 3680 (2014).
- V. Sunko, F. Mazzola, S. Kitamura, S. Khim, P. Kushwaha, O. J. Clark, M. D. Watson, I. Marković, D. Biswas, L. Pourovskii, T. K. Kim, T. L. Lee, P. K. Thakur, H. Rosner, A. Georges, R. Moessner, T. Oka, A. P. Mackenzie, and P. D. C. King, "Probing spin correlations using angle-resolved photoemission in a coupled metallic/Mott insulator system," *Sci. Adv.* **6**, eaaz0611 (2020).
- M. D. Le, S. Jeon, A. I. Kolesnikov, D. J. Voneshen, A. S. Gibbs, J. S. Kim, J. Jeong, H. J. Noh, C. Park, J. Yu, T. G. Perring, and J. G. Park, "Magnetic interactions in PdCrO₂ and their effects on its magnetic structure," *Phys. Rev. B* **98**, 024429 (2018).
- B. Burganov, C. Adamo, A. Mulder, M. Uchida, P. D. C. King, J. W. Harter, D. E. Shai, A. S. Gibbs, A. P. Mackenzie, R. Uecker, M. Bruetzam, M. R. Beasley, C. J. Fennie, D. G. Schlom, and K. M. Shen, "Strain control of fermiology and many-body interactions in two-dimensional ruthenates," *Phys. Rev. Lett.* **116**, 197003 (2016).
- J. P. Ruf, H. Paik, N. J. Schreiber, H. P. Nair, L. Miao, J. K. Kawasaki, J. N. Nelson, B. D. Faeth, Y. Lee, B. H. Goodge, B. Pamuk, C. J. Fennie, L. F. Kourkoutis, D. G. Schlom, and K. M. Shen, "Strain-stabilized superconductivity," *Nat. Commun.* **12**, 59 (2021).

- ¹⁷P. D. C. King, H. I. Wei, Y. F. Nie, M. Uchida, C. Adamo, S. Zhu, X. He, I. Božović, D. G. Schlom, and K. M. Shen, "Atomic-scale control of competing electronic phases in ultrathin LaNiO_3 ," *Nat. Nanotechnol.* **9**, 443–447 (2014).
- ¹⁸J. K. Kawasaki, C. H. Kim, J. N. Nelson, S. Crisp, C. J. Zollner, E. Biegenwald, J. T. Heron, C. J. Fennie, D. G. Schlom, and K. M. Shen, "Engineering carrier effective masses in ultrathin quantum wells of IrO_2 ," *Phys. Rev. Lett.* **121**, 176802 (2018).
- ¹⁹C. T. Parzyck, A. Galdi, J. K. Nangoi, W. J. I. DeBenedetti, J. Balajka, B. D. Faeth, H. Paik, C. Hu, T. A. Arias, M. A. Hines, D. G. Schlom, K. M. Shen, and J. M. Maxson, "Single-crystal alkali antimonide photocathodes: High efficiency in the ultrathin limit," *Phys. Rev. Lett.* **128**, 114801 (2022).
- ²⁰J. K. Kawasaki, M. Uchida, H. Paik, D. G. Schlom, and K. M. Shen, "Evolution of electronic correlations across the rutile, perovskite, and Ruddeldsen-Popper iridates with octahedral connectivity," *Phys. Rev. B* **94**, 121104 (2016).
- ²¹J. K. Kawasaki, D. Baek, H. Paik, H. P. Nair, L. F. Kourkoutis, D. G. Schlom, and K. M. Shen, "Rutile $\text{IrO}_2/\text{TiO}_2$ superlattices: A hyperconnected analog to the Ruddeldsen-Popper structure," *Phys. Rev. Mater.* **2**, 054206 (2018).
- ²²J. N. Nelson, N. J. Schreiber, A. B. Georgescu, B. H. Goodge, B. D. Faeth, C. T. Parzyck, C. Zeledon, L. F. Kourkoutis, A. J. Millis, A. Georgescu, D. G. Schlom, and K. M. Shen, "Interfacial charge transfer and persistent metallicity of ultrathin $\text{SrIrO}_3/\text{SrRuO}_3$ heterostructures," *Sci. Adv.* **8**, eabj0481 (2022).
- ²³Q. Song, T. L. Yu, X. Lou, B. P. Xie, H. C. Xu, C. H. P. Wen, Q. Yao, S. Y. Zhang, X. T. Zhu, J. D. Guo, R. Peng, and D. L. Feng, "Evidence of cooperative effect on the enhanced superconducting transition temperature at the $\text{FeSe}/\text{SrTiO}_3$ interface," *Nat. Commun.* **10**, 758 (2019).
- ²⁴J. W. Harter, L. Maritato, D. E. Shai, E. J. Monkman, Y. Nie, D. G. Schlom, and K. M. Shen, "Nodeless superconducting phase arising from a strong (π , π) antiferromagnetic phase in the infinite-layer electron-doped $\text{Sr}_{1-x}\text{La}_x\text{CuO}_2$ compound," *Phys. Rev. Lett.* **109**, 267001 (2012).
- ²⁵J. W. Harter, L. Maritato, D. E. Shai, E. J. Monkman, Y. Nie, D. G. Schlom, and K. M. Shen, "Doping evolution and polar surface reconstruction of the infinite-layer cuprate $\text{Sr}_{1-x}\text{La}_x\text{CuO}_2$," *Phys. Rev. B* **92**, 035149 (2015).
- ²⁶Y. F. Nie, D. Di Sante, S. Chatterjee, P. D. C. King, M. Uchida, S. Ciuchi, D. G. Schlom, and K. M. Shen, "Formation and observation of a quasi-two-dimensional d_{xy} electron liquid in epitaxially stabilized $\text{Sr}_{2-x}\text{La}_x\text{TiO}_4$ thin films," *Phys. Rev. Lett.* **115**, 096405 (2015).
- ²⁷H. I. Wei, C. Adamo, E. A. Nowadnick, E. B. Lochocki, S. Chatterjee, J. P. Ruf, M. R. Beasley, D. G. Schlom, and K. M. Shen, "Electron doping of the parent cuprate La_2CuO_4 without cation substitution," *Phys. Rev. Lett.* **117**, 147002 (2016).
- ²⁸E. B. Lochocki, H. Paik, M. Uchida, D. G. Schlom, and K. M. Shen, "Controlling surface carrier density by illumination in the transparent conductor La-doped BaSnO_3 ," *Appl. Phys. Lett.* **112**, 181603 (2018).
- ²⁹J. N. Nelson, C. T. Parzyck, B. D. Faeth, J. K. Kawasaki, D. G. Schlom, and K. M. Shen, "Mott gap collapse in lightly hole-doped $\text{Sr}_{2-x}\text{K}_x\text{IrO}_4$," *Nat. Commun.* **11**, 2597 (2020).
- ³⁰T. Harada, S. Ito, and A. Tsukazaki, "Electric dipole effect in $\text{PdCoO}_2/\beta\text{-Ga}_2\text{O}_3$ Schottky diodes for high-temperature operation," *Sci. Adv.* **5**, eaax573 (2019).
- ³¹J. H. Lee, T. Harada, F. Trier, L. Marcano, F. Godel, S. Valencia, A. Tsukazaki, and M. Bibes, "Nonreciprocal transport in a Rashba ferromagnet, delafossite PdCoO_2 ," *Nano Lett.* **21**, 8687–8692 (2021).
- ³²P. F. Carcia, R. D. Shannon, P. E. Bierstedt, and R. B. Flippen, " O_2 electrocatalysis on thin film metallic oxide electrodes with the delafossite structure," *J. Electrochem. Soc.* **127**, 1974–1978 (1980).
- ³³T. Harada, K. Fujiwara, and A. Tsukazaki, "Highly conductive PdCoO_2 ultrathin films for transparent electrodes," *APL Mater.* **6**, 046107 (2018).
- ³⁴P. Yordanov, W. Sigle, P. Kaya, M. E. Gruner, R. Pentcheva, B. Keimer, and H.-U. Habermeier, "Large thermopower anisotropy in PdCoO_2 thin films," *Phys. Rev. Mater.* **3**, 085403 (2019).
- ³⁵J. M. Ok, M. Brahlek, W. S. Choi, K. M. Roccapriore, M. F. Chisholm, S. Kim, C. Sohn, E. Skoropata, S. Yoon, J. S. Kim, and H. N. Lee, "Pulsed-laser epitaxy of metallic delafossite PdCrO_2 films," *APL Mater.* **8**, 051104 (2020).
- ³⁶T. Miyakawa, T. Harada, S. Ito, and A. Tsukazaki, "Inhomogeneous interface dipole effect at the Schottky junctions of PdCrO_2 on $\beta\text{-Ga}_2\text{O}_3$ (201) substrates," *J. Appl. Phys.* **128**, 025302 (2020).
- ³⁷M. Brahlek, G. Rimal, J. M. Ok, D. Mukherjee, A. R. Mazza, Q. Lu, H. N. Lee, T. Z. Ward, R. R. Unocic, G. Eres, and S. Oh, "Growth of metallic delafossite PdCoO_2 by molecular beam epitaxy," *Phys. Rev. Mater.* **3**, 093401 (2019).
- ³⁸J. Sun, M. R. Barone, C. S. Chang, M. E. Holtz, H. Paik, J. Schubert, D. A. Muller, and D. G. Schlom, "Growth of PdCoO_2 by ozone-assisted molecular-beam epitaxy," *APL Mater.* **7**, 121112 (2019).
- ³⁹T. Harada, K. Sugawara, K. Fujiwara, M. Kitamura, S. Ito, T. Nojima, K. Horiba, H. Kumigashira, T. Takahashi, T. Sato, and A. Tsukazaki, "Anomalous Hall effect at the spontaneously electron-doped polar surface of PdCoO_2 ultrathin films," *Phys. Rev. Res.* **2**, 013282 (2020).
- ⁴⁰H.-J. Noh, J. Jeong, J. Jeong, E.-J. Cho, S. B. Kim, K. Kim, B. I. Min, and H.-D. Kim, "Anisotropic electric conductivity of delafossite PdCoO_2 studied by angle-resolved photoemission spectroscopy," *Phys. Rev. Lett.* **102**, 256404 (2009).
- ⁴¹F. Mazzola, V. Sunko, S. Khim, H. Rosner, P. Kushwaha, O. J. Clark, L. Bawden, I. Marković, T. K. Kim, M. Hoesch, A. P. Mackenzie, and P. D. C. King, "Itinerant ferromagnetism of the Pd-terminated polar surface of PdCoO_2 ," *Proc. Natl. Acad. Sci. U. S. A.* **115**, 12956–12960 (2018).
- ⁴²V. Sunko, *Angle Resolved Photoemission Spectroscopy of Delafossite Metals*, 1st ed. (Springer, Cham, 2019).
- ⁴³N. Terada, Y. Ikedo, H. Sato, D. D. Khalyavin, P. Manuel, F. Orlandi, Y. Tsujimoto, Y. Matsushita, A. Miyake, A. Matsuo, M. Tokunaga, and K. Kindo, "Difference in magnetic and ferroelectric properties between rhombohedral and hexagonal polytypes of AgFeO_2 : A single-crystal study," *Phys. Rev. B* **99**, 064402 (2019).
- ⁴⁴N. Terada, D. D. Khalyavin, P. Manuel, Y. Tsujimoto, K. Knight, P. G. Radaelli, H. S. Suzuki, and H. Kitazawa, "Spiral-spin-driven ferroelectricity in a multiferroic delafossite AgFeO_2 ," *Phys. Rev. Lett.* **109**, 097203 (2012).
- ⁴⁵K. P. Ong, K. Bai, P. Blaha, and P. Wu, "Electronic structure and optical properties of AFeO_2 (A = Ag, Cu) within GGA calculations," *Chem. Mater.* **19**, 634–640 (2007).
- ⁴⁶M. V. Limaye, M. Pramanik, S. B. Singh, G. R. Paik, and P. Singh, "Application of delafossite AgFeO_2 nanoparticles as SERS substrate and antimicrobial agent," *ChemistrySelect* **6**, 2678–2686 (2021).
- ⁴⁷M. A. Marquardt, N. A. Ashmore, and D. P. Cann, "Crystal chemistry and electrical properties of the delafossite structure," *Thin Solid Films* **496**, 146–156 (2006).
- ⁴⁸B. V. Beznosikov and K. S. Aleksandrov, "Predictions of compounds in the family of delafossites," *J. Struct. Chem.* **50**, 102–107 (2009).
- ⁴⁹T. F. T. Cerqueira, S. Lin, M. Amsler, S. Goedecker, S. Botti, and M. A. L. Marques, "Identification of novel Cu, Ag, and Au ternary oxides from global structural prediction," *Chem. Mater.* **27**, 4562–4573 (2015).
- ⁵⁰J. Shi, T. F. T. Cerqueira, W. Cui, F. Nogueira, S. Botti, and M. A. L. Marques, "High-throughput search of ternary chalcogenides for p-type transparent electrodes," *Sci. Rep.* **7**, 43179 (2017).
- ⁵¹W. A. Jesser, "A theory of pseudomorphism in thin films," *Mater. Sci. Eng.* **4**, 279–286 (1969).
- ⁵²E. Machlin and P. Chaudhari, "Theory of 'pseudomorphic stabilization' of metastable phases in thin film form," in *Synthesis and Properties of Metastable Phases*, edited by E. S. machlin and T. J. rowland (The Metallurgical Society of AIM, Warrendale, 1980), pp. 11–29.
- ⁵³C. P. Flynn, "Strain-assisted epitaxial growth of new ordered compounds," *Phys. Rev. Lett.* **57**, 599–602 (1986).
- ⁵⁴R. Bruinsma and A. Zangwill, "Structural transitions in epitaxial overlayers," *J. Phys.* **47**, 2055–2073 (1986).
- ⁵⁵A. Zunger and D. M. Wood, "Structural phenomena in coherent epitaxial solids," *J. Cryst. Growth* **98**, 1–17 (1989).
- ⁵⁶A. R. Kaul, O. Y. Gorbenko, and A. A. Kamenev, "The role of heteroepitaxy in the development of new thin-film oxide-based functional materials," *Russ. Chem. Rev.* **73**, 861–880 (2004).
- ⁵⁷H. Takatsu, J. J. Ishikawa, S. Yonezawa, H. Yoshino, T. Shishidou, T. Oguchi, K. Murata, and Y. Maeno, "Extremely large magnetoresistance in the nonmagnetic metal PdCoO_2 ," *Phys. Rev. Lett.* **111**, 056601 (2013).
- ⁵⁸N. Nandi, T. Scaffidi, P. Kushwaha, S. Khim, M. E. Barber, V. Sunko, F. Mazzola, P. D. C. King, H. Rosner, P. J. W. Moll, M. König, J. E. Moore, S. Hartnoll, and A. P. Mackenzie, "Unconventional magneto-transport in ultrapure PdCoO_2 and PtCoO_2 ," *npj Quantum Mater.* **3**, 66 (2018).

Supplementary material for "Growth of PdCoO₂ films with controlled termination by molecular-beam epitaxy and determination of their electronic structure by angle-resolved photoemission spectroscopy"

Qi Song,¹ Jiaxin Sun,¹ Christopher T. Parzyck,² Ludi Miao,² Qing Xu,³ Felix V.E. Hensling,¹ Matthew R. Barone,¹ Cheng Hu,¹ Jinkwon Kim,¹ Brendan D. Faeth,³ Hanjong Paik,³ Phil D. C. King,⁴ Kyle M. Shen,^{2,5} and Darrell G. Schlom^{1,5,6}

¹*Department of Materials Sciences and Engineering, Cornell University, Ithaca, New York 14853, USA*

²*Department of Physics, Laboratory of Atomic and Solid State Physics, Cornell University, Ithaca, New York 14853, USA*

³*Platform for the Accelerated Realization, Analysis, and Discovery of Interface Materials (PARADIM), Cornell University, Ithaca, New York 14853, USA*

⁴*SUPA, School of Physics and Astronomy, University of St Andrews, St Andrews KY16 9SS, UK*

⁵*Kavli Institute at Cornell for Nanoscale Science, Ithaca, New York 14853, USA*

⁶*Leibniz-Institut für Kristallzüchtung, Max-Born-Straße 2, 12489 Berlin, Germany*

A. Composition control methods for growth of PdCoO₂ films

Building upon our previous work,¹ thin films of PdCoO₂ were synthesized by reactive oxide molecular-beam epitaxy (MBE) in a Veeco GEN-10 MBE system on (001) sapphire substrates. The substrates were heated to temperatures in the 500 °C to 580 °C range as determined by a thermocouple close to, but not in contact with the substrate heater. A mixture of approximately 80% ozone and 20% oxygen at a background pressure of 5×10^{-6} to 8.5×10^{-6} Torr was used during deposition. The fluxes of palladium, cobalt, and iron evaporated from MBE effusion cells were each set to provide a flux of around 1×10^{13} atoms·cm²/sec using a quartz crystal microbalance. This initial calibration was then refined by measuring the thickness of a palladium calibration film grown on a (111) (ZrO₂)_{0.905}(Y₂O₃)_{0.09} substrate, a Co₃O₄ calibration film grown on a (100) MgAl₂O₄ substrate, and an Fe₂O₃ calibration film grown on a (001) Al₂O₃ substrate.²

Epitaxial PdCoO₂ films were grown in two different ways. In the first method, the palladium and cobalt shutters were actuated to supply monolayer doses of palladium and cobalt following the sequence of atomic layers along the *c*-axis of the crystal structure of PdCoO₂, as well as the film termination layer. We refer to this method as "shutter-controlled growth," and results from this method are shown in Fig. S1. Under a continuous ozone flux, growth is initiated with the CoO₂ monolayer. The first fourteen alternating monolayers (containing seven formula units PdCoO₂) are grown assuming unity sticking coefficients of cobalt and palladium, i.e., a Pd:Co ratio of 1:1. After the deposition of seven formula units, 20% excess palladium is supplied in each shuttered dose, i.e., a Pd:Co ratio of 1.2:1.¹ The excess palladium supplied in each shuttered dose is to make up for the evaporation of palladium oxide at the relatively high substrate temperature and ozone pressure used.³ The flux of iron was adjusted according to the desired film composition assuming that the sticking coefficient of iron is unity.

The second method we have used to grow single-phase epitaxial PdCoO₂ films involves the codeposition of cobalt, palladium, and ozone under conditions that the excess palladium supplied desorbs as PdO (g). We refer this method as "absorption-controlled growth," and results using this method are shown in Fig. S2.

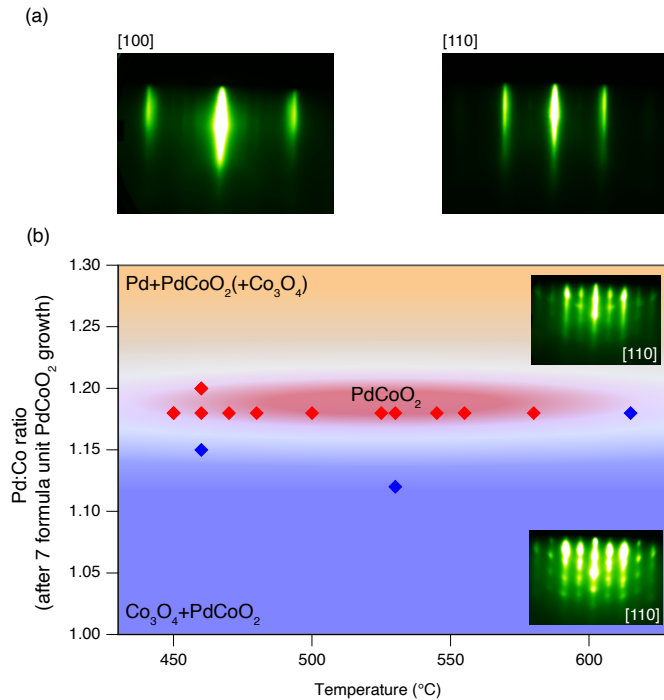


FIG. S1. **Shutter-controlled growth of PdCoO₂**. Here shutters are used to provide monolayer doses following the sequence of atomic layers along the *c*-axis of the PdCoO₂ crystal structure. All of the films in the main text are grown by this method. The first seven formula units of PdCoO₂ are grown with a ratio of Pd:Co = 1:1 after which 20% excess palladium is supplied to make up for the evaporation of palladium oxide. (a) RHEED patterns of a seven formula-unit-thick PdCoO₂ film grown at 530 °C viewed along the indicated azimuths. Note that the first seven formula units of PdCoO₂ grown with Pd:Co = 1:1 are extremely sensitive to the incident fluxes. Slight variation from the stoichiometric composition can induce impurity phases and compromise later growth. With precise composition control, the growth window of the substrate temperature can vary from 450 °C to 600 °C. (b) Diagram showing the phases observed in grown films as a function of the Pd:Co ratio and growth temperature under a constant ozone background pressure of 5×10^{-6} Torr. All of the data points here are starting with single-phase seven formula-unit-thick PdCoO₂. The red dots indicate phase-pure PdCoO₂ films while blue dots represent films that contain PdCoO₂ but are not phase pure. Although excess palladium is supplied during the growth of the thicker films, the excess ratio of Pd:Co is still essential to the growth. If the ratio is less than 1.18, the film tends to form Co₃O₄ as an impurity phase. On the other hand, if the ratio is larger than 1.2, the extra palladium tends to form palladium metal as an impurity phase, usually accompanied by the Co₃O₄ phase. The insets show RHEED patterns containing the impurity phase of palladium metal (top) and Co₃O₄ (bottom). Even with the precise excess Pd:Co ratio, the growth temperature of PdCoO₂ is still limited to the range of 450 °C to 600 °C; higher growth temperature can result in single-phase Co₃O₄ films.

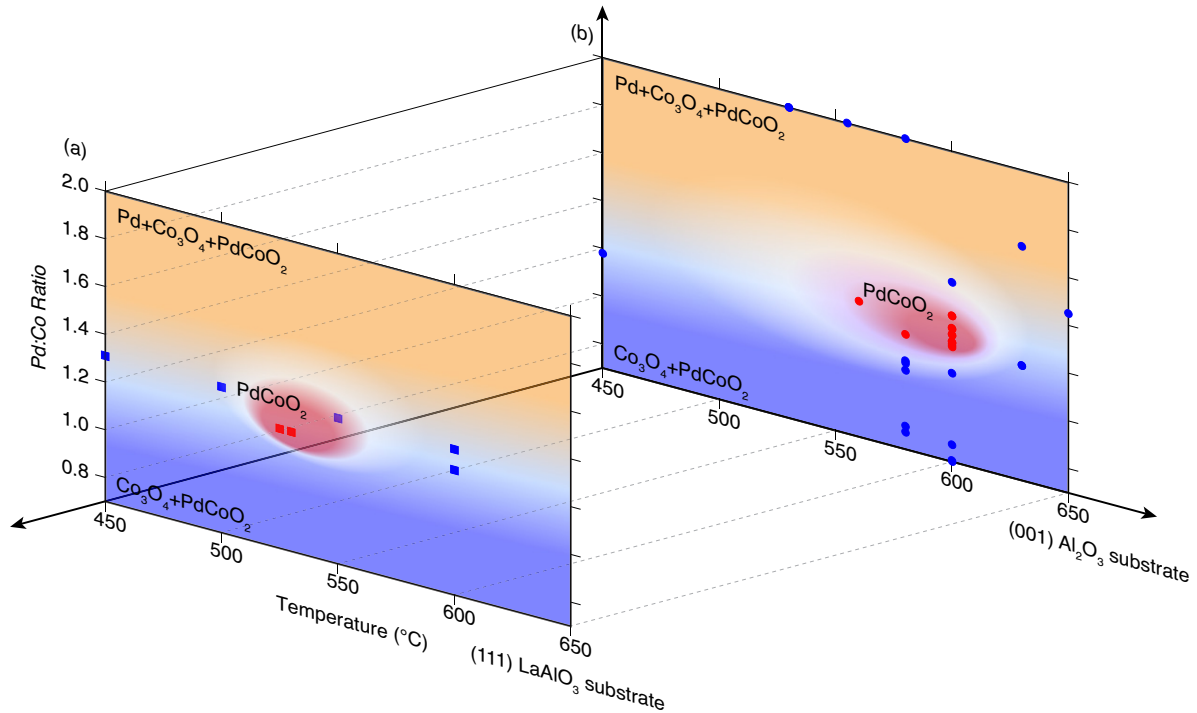


FIG. S2. The absorption-controlled growth method exploits volatility differences between the constituents elements to produce a single-phase film within a limited range of growth conditions referred to as a growth window. Here, all of the elements are supplied at the same time and thermodynamics provides automatic composition control within a growth window, resulting in phase-pure PdCoO₂ films. Unfortunately, the termination layer of the film usually turns out to be a mixture of the palladium and CoO₂ monolayers. All the films described here are initiated with one monolayer of CoO₂. Diagrams showing the phases observed in the codeposited films as a function of substrate temperature and Pd:Co ratio for films deposited on (a) (001) Al₂O₃ substrates and on (b) (111) LaAlO₃ substrates. The red dots indicate phase-pure PdCoO₂ films, while the blue dots indicate PdCoO₂ films containing additional phases, usually CoO₂ or palladium. For PdCoO₂ growth by absorption control, the growth window of temperature is smaller compared to that of shutter-controlled growth, but the absolute temperature of the growth window is hotter. The flux ratio of Pd:Co can extend from 1.12 to 1.3. For PdCoO₂ films grown on (111) LaAlO₃ substrates, the similarly narrow growth window is about 70 °C lower than for growth on (001) Al₂O₃ substrates.

B. Atomic force microscopy for different terminations of PdCoO₂ films grown on (001) Al₂O₃ substrates

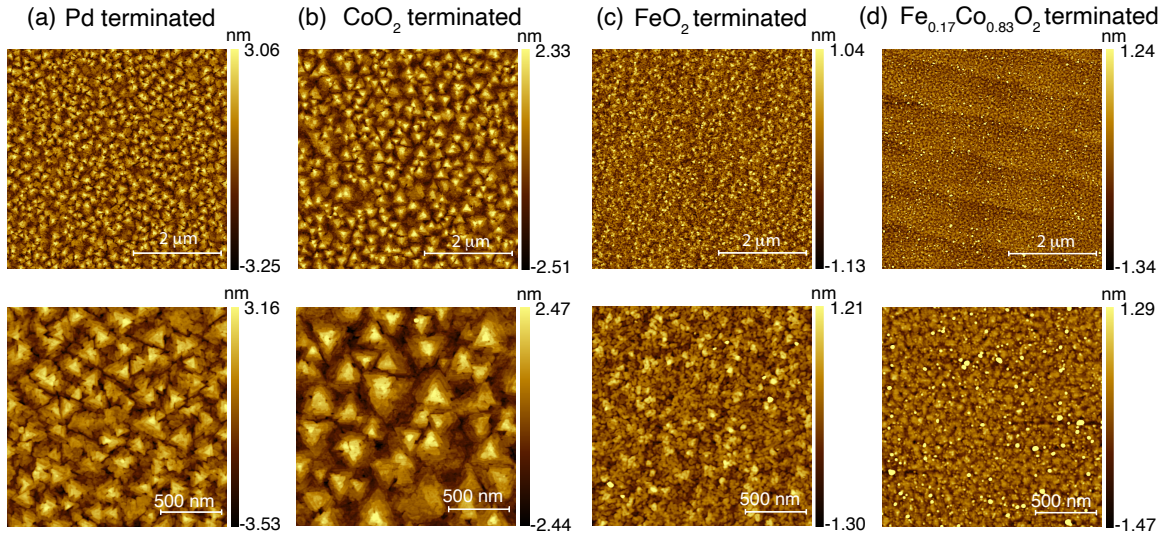


FIG. S3. Atomic force microscopy (AFM) images of differently terminated PdCoO₂ films: (a) Pd-terminated; (b) CoO₂-terminated; (c) FeO₂-terminated; and (d) Fe_{0.17}Co_{0.83}O₂-terminated. All of the films are around 13 nm thick.

C. Surface reconstruction of PdCoO₂ film grown on a (001) Al₂O₃ substrate

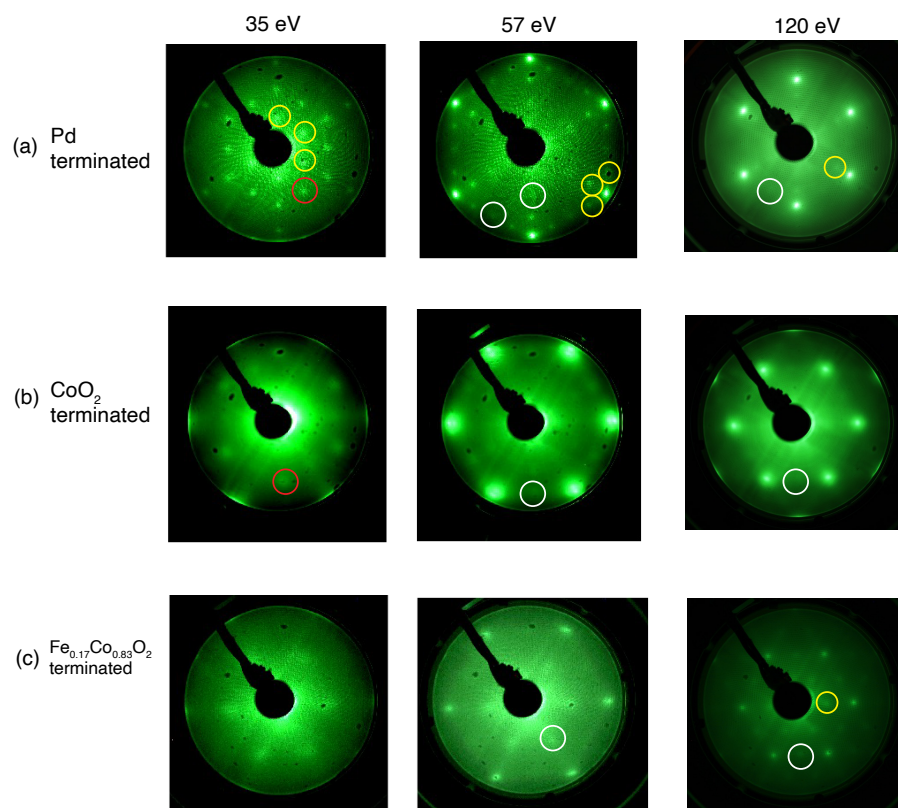


FIG. S4. Low-energy electron diffraction (LEED) pattern of differently terminated PdCoO₂ films at different energies: (a) Pd-terminated; (b) CoO₂-terminated; and (c) Fe_{0.17}Co_{0.83}O₂-terminated. Distinct reconstructions corresponding to the white, yellow, and red sets of spots are illustrated.

D. Electronic structure

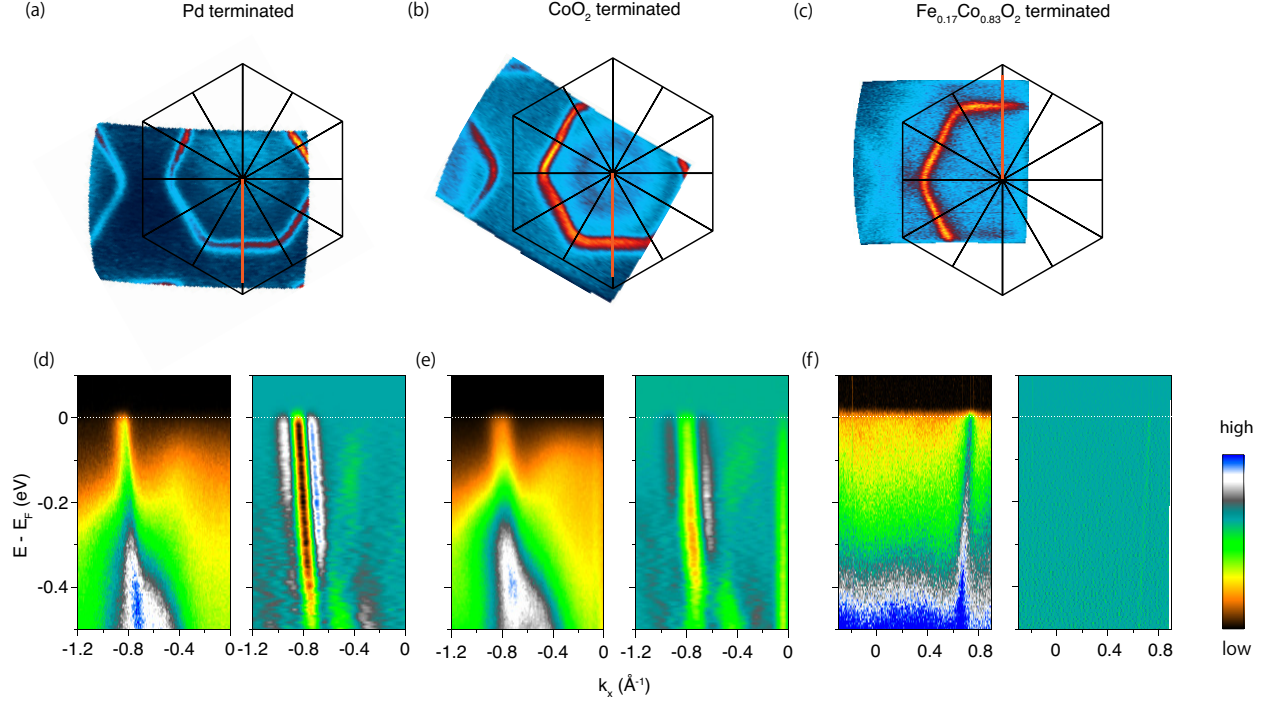


FIG. S5. **Photoemission intensity maps of differently terminated PdCoO_2 films measured at a photon energy of 40.4 eV.** Photoemission intensity mapping of a (a) Pd-terminated, (b) CoO_2 -terminated, and (c) $\text{Fe}_{0.17}\text{Co}_{0.83}\text{O}_2$ -terminated PdCoO_2 films. (d) Photoemission intensity distributions across Γ -K along the orange cut illustrated in Fig. 3(j) of a Pd-terminated PdCoO_2 film and its second derivative with respect to energy. The Pd-terminated surface state is more pronounced when measured at this photon energy. (e),(f) are the same as (d), but taken from a CoO_2 -terminated PdCoO_2 film and a $\text{Fe}_{0.17}\text{Co}_{0.83}\text{O}_2$ -terminated PdCoO_2 film, respectively.

Name of band	v_F from parabolic fitting ($\text{eV} \cdot \text{\AA}$)	v_F from linear fitting ($\text{eV} \cdot \text{\AA}$)
Bulk state	3.54 ± 0.35	4.32 ± 0.25
Surface state 1	0.75 ± 0.07	0.79 ± 0.11
Surface state 2	0.47 ± 0.02	0.53 ± 0.03

TABLE S1. Different fitting results of v_F in the CoO_2 -terminated PdCoO_2 film as shown in Fig. 3.

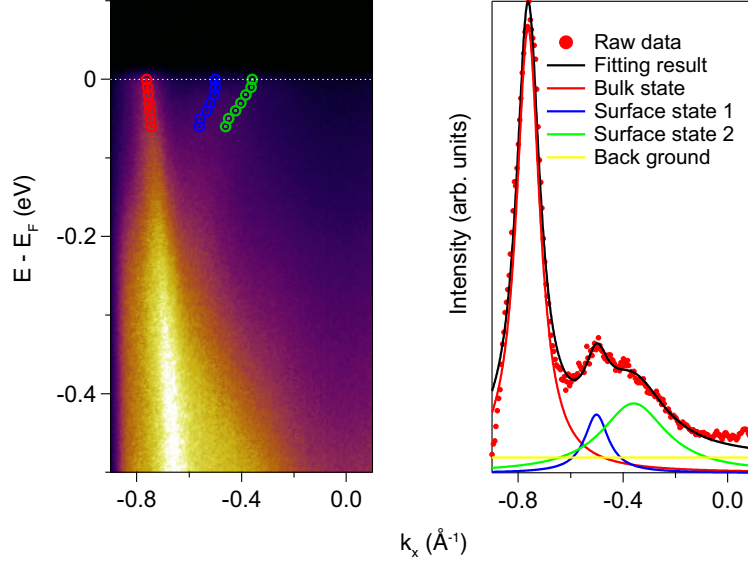


FIG. S6. Fermi velocity (v_F) fitting of the PdCoO₂ bulk state and surface states, respectively. Momentum dispersion curves (MDCs) near E_F are used to obtain v_F . Lorentz peaks are used to find the momentum of these bands. Linear fitting and parabolic fitting of the peak positions are applied and give rise to similar results as shown in Table S1. We use linear fitting in the main text.

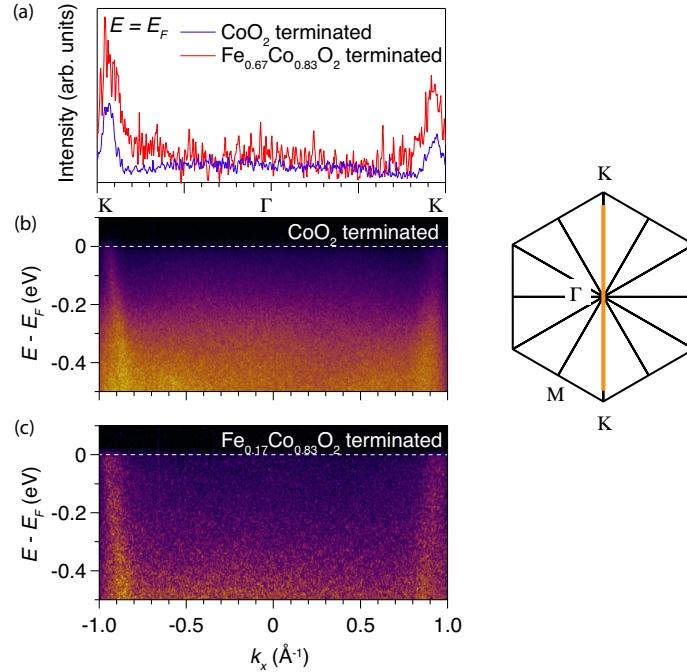


FIG. S7. Comparison of MDCs along K- Γ -K direction at E_F of (a) a 5 nm thick PdCoO₂ film and of (b) a 13 nm thick PdFe_{0.17}Co_{0.83}O₂ film. Data were taken at He-II photo energy (40.4 eV) at 6 K. Momentum at E_F of the PdCoO₂ film and the PdFe_{0.17}Co_{0.83}O₂ film shows no obvious difference.

E. X-Ray Photoelectron Spectroscopy

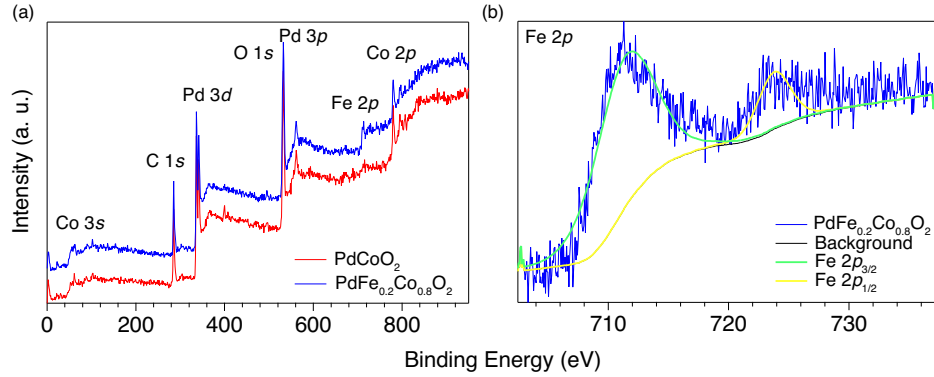


FIG. S8. (a) The results of x-ray photoelectron spectroscopy for a 12 nm thick PdCoO₂ film and a 12 nm thick PdFe_{0.2}Co_{0.8}O₂ film. Fe 2*p* peaks are shown in the PdFe_{0.2}Co_{0.8}O₂ film. (b) Fine scan of Fe 2*p* peaks of the PdFe_{0.2}Co_{0.8}O₂ film. Due to the instrumental resolution and limited amount of iron present in the sample, it is difficult to assign the Fe 2*p* peaks to a particular iron oxide oxidation state (e.g., Fe³⁺ or Fe²⁺ behavior). (The Fe 2*p*_{3/2} peaks show Fe³⁺ behavior and the Fe 2*p*_{1/2} peaks show a combination of Fe³⁺ and Fe²⁺ behavior.)^{4,5} Data are taken at room temperature.

F. Hall effect

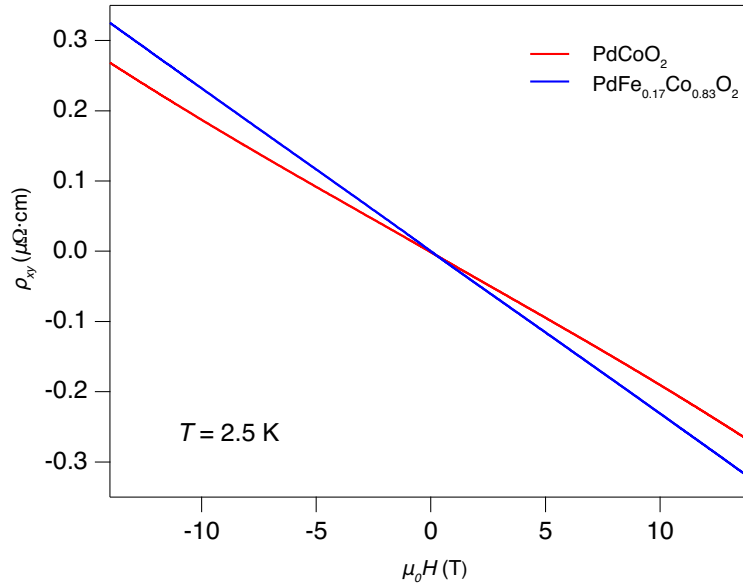


FIG. S9. The Hall resistivity ρ_{xy} for the PdCoO_2 film and the $\text{PdFe}_{0.17}\text{Co}_{0.83}\text{O}_2$ film shown in Fig. 6 of the main text at 2.5 K. The Data are antisymmetrized to get rid of the longitudinal component. The magnetic field H (in the range of ± 14 T) is applied parallel to the c axis. The magnetic field H applied in Fig. 6(a) of the main text is in the range of ± 1 T.

G. Magnetization

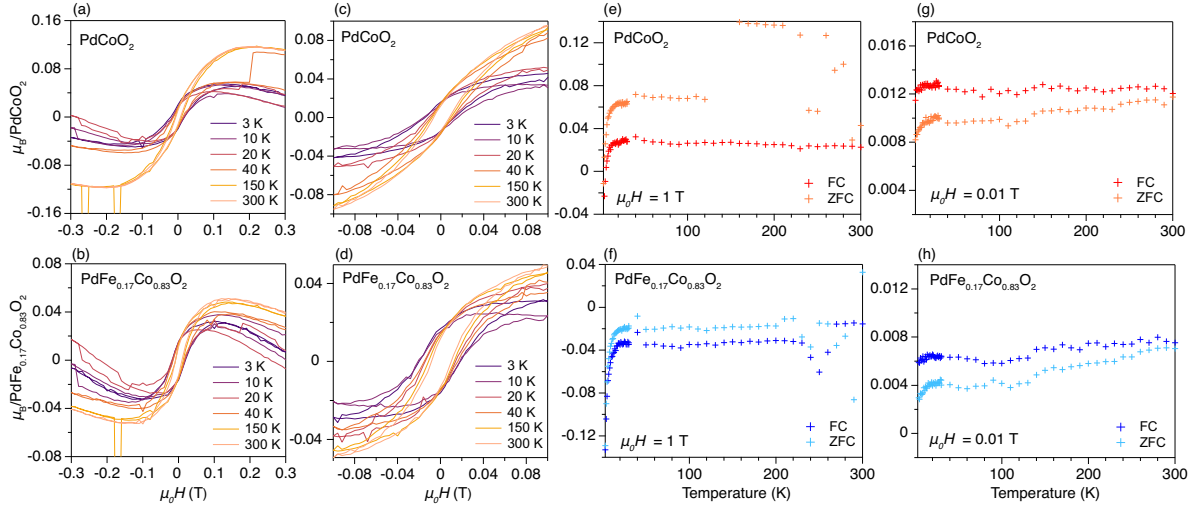


FIG. S10. (a),(b) Temperature dependence of magnetization vs magnetic field for a 12.5 nm thick PdCoO₂ film and a 12.8 nm thick PdFe_{0.17}Co_{0.83}O₂ film, respectively. (c),(d) The same as (a) and (b), but these scans are made on a finer scale at small magnetic field. (e),(g) Zero-field-cooled (ZFC) and field-cooled (FC) curves showing the temperature dependence of the magnetic susceptibility in the (001) plane of the PdCoO₂ film under an applied magnetic field of 1 T and 0.01 T, respectively. (f),(h) The same as (e) and (g), but for the PdFe_{0.17}Co_{0.83}O₂ film. Measurements are made using a Quantum Design MPMS3 SQUID magnetometer. Prior to the magnetization measurements, the backside coating of platinum (with a thin titanium adhesion layer) was mechanically removed so that only the PdCoO₂ and PdFe_{0.17}Co_{0.83}O₂ films, respectively, measured. Further, the contribution from sapphire substrate was subtracted prior to plotting to show the behavior of just the films. To properly normalize the signal from the bare sapphire substrate (from the same batch of the substrates from the same vendor), the samples and the substrate were weighed.

REFERENCES

- ¹J. Sun, M. R. Barone, C. S. Chang, M. E. Holtz, H. Paik, J. Schubert, D. A. Muller, and D. G. Schlom, “Growth of PdCoO₂ by ozone-assisted molecular-beam epitaxy,” *APL Mater.* **7**, 121112 (2019).
- ²J. Sun, C. T. Parzyck, J. H. Lee, C. M. Brooks, L. F. Kourkoutis, X. Ke, R. Misra, J. Schubert, F. V. Hensling, M. R. Barone, Z. Wang, M. E. Holtz, N. J. Schreiber, Q. Song, H. Paik, T. Heeg, D. A. Muller, K. M. Shen, and D. G. Schlom, “Canonical approach to cation flux calibration in oxide molecular-beam epitaxy,” *Phys. Rev. Mater.* **6**, 033802 (2022).
- ³K. M. Adkison, S. L. Shang, B. J. Bocklund, D. Klimm, D. G. Schlom, and Z. K. Liu, “Suitability of binary oxides for molecular-beam epitaxy source materials: A comprehensive thermodynamic analysis,” *APL Mater.* **8**, 081110 (2020).
- ⁴R. Tang, C. Jiang, W. Qian, J. Jian, X. Zhang, H. Wang, and H. Yang, “Dielectric relaxation, resonance and scaling behaviors in Sr₃Co₂Fe₂₄O₄₁ hexaferrite,” *Sci. Rep.* **5**, 13645 (2015).
- ⁵C. Yu, Y. Zeng, B. Yang, R. Wylde, R. Donnan, J. Wu, J. Xu, F. Gao, I. Abrahams, M. Reece, and H. Yan, “SrFe₁₂O₁₉ based ceramics with ultra-low dielectric loss in the millimetre-wave band,” *Appl. Phys. Lett.* **112**, 143501 (2018).